Basic Proline-Rich Protein-Mediated Microtubules Are Essential for Lobe Growth and Flattened Cell Geometry[1]

Jeh Haur Wong,[a,2,3] Takehide Kato,[a,2] Samuel A. Belteton,[b] Rie Shimizu,[a] Nene Kinoshita,[a] Takumi Higaki,[c] Yuichi Sakumura,[a] Daniel B. Szymanski,[b,d] and Takashi Hashimoto[a,4,5]

[a]Graduate School of Science and Technology, Nara Institute of Science and Technology, Ikoma, Nara 630-0192, Japan
[b]Department of Botany and Plant Pathology, Purdue University, West Lafayette, Indiana 47907
[c]International Research Organization for Advanced Science and Technology, Kumamoto University, Kumamoto 860-8555, Japan
[d]Department of Biological Sciences, Purdue University, West Lafayette, Indiana 47907

ORCID IDs: 0000-0002-3697-6051 (J.H.W.); 0000-0003-3733-4824 (S.A.B.); 0000-0001-8255-424X (D.B.S.); 0000-0002-8398-5479 (T.Ha.).

Complex cell shapes are generated first by breaking symmetry, and subsequent polar growth. Localized bending of anticlinal walls initiates lobe formation in the epidermal pavement cells of cotyledons and leaves, but how the microtubule cytoskeleton mediates local cell growth, and how plant pavement cells benefit from adopting jigsaw puzzle-like shapes, are poorly understood. In Arabidopsis (*Arabidopsis thaliana*), the basic Pro-rich protein (BPP) microtubule-associated protein family comprises seven members. We analyzed lobe morphogenesis in cotyledon pavement cells of a *BPP1;BPP2;BPP5* triple knockout mutant. New image analysis methods (MtCurv and BQuant) showed that anticlinal microtubule bundles were significantly reduced and cortical microtubules that fan out radially across the periclinal wall did not enrich at the convex side of developing lobes. Despite these microtubule defects, new lobes were initiated at the same frequency as in wild-type cells, but they did not expand into well-defined protrusions. Eventually, mutant cells formed nearly polygonal shapes and adopted concentric microtubule patterns. The mutant periclinal cell wall bulged outward. The radius of the calculated inscribed circle of the pavement cells, a proposed proxy for maximal stress in the cell wall, was consistently larger in the mutant cells during cotyledon development, and correlated with an increase in cell height. These *bpp* mutant phenotypes provide genetic and cell biological evidence that initiation and growth of lobes are distinct morphogenetic processes, and that interdigitated cell geometry effectively suppresses large outward bulging of pavement cells.

Starting from small polyhedral cells just after cell division, interphase plant cells undergo striking changes in size and shape. For instance, pavement cells of the leaf and cotyledon epidermis mature into complex morphologies, typically seen as interdigitated jigsaw puzzle-like shapes in vascular plants (Panteris and Galatis, 2005; Vőfély et al., 2019). In cotyledons of Arabidopsis (*Arabidopsis thaliana*), a representative species with high pavement cell interdigitation (Vőfély et al., 2019), an initial wave of lobe initiation occurs until ~2 d after germination (DAG; Zhang et al., 2011; Armour et al., 2015; Wu et al., 2016; Möller et al., 2017). After an extended phase of relatively isotropic cell expansion at ~3 DAG, additional lobes are formed (Zhang et al., 2011). In the cell segment that forms a new lobe, only a small subregion of the cell protrudes at the time scale of hours to generate a small (~200 nm) local defection in the cell boundary, which is propagated and elaborated for days to generate a tissue composed of highly interdigitated cells (Zhang et al., 2011; Belteton et al., 2018). There must be local differences in the rates and directions of cell wall expansion where the lobe is initiated.

Because lobe formation occurs in the context of a tissue of mechanically coupled cells, the growth

[1]This work was supported by Grant-in-Aid for Scientific Research on Innovative Areas from the Ministry of Education, Culture, Sports, Science and Technology, Japan (grant no. 24114004 to T.Ha.); Grant-in-Aid for Scientific Research on Challenging Research (Exploratory) from the Ministry of Education, Culture, Sports, Science and Technology, Japan (grant no. 17K19380 to T.Hi.); by the Creation of Industrial Infrastructure Research Grant from Canon Foundation (to T.Hi.); and by the US National Science Foundation, Division of Molecular and Cellular Biosciences (grant no. 1715544 to D.B.S.).

[2]These authors contributed equally to this work.

[3]Present address: Department of Plant and Microbial Biology, University of Minnesota, St. Paul, Minnesota 55108.

[4]Author for contact: hasimoto@bs.naist.jp.

[5]Senior author.

The author responsible for distribution of materials integral to the findings presented in this article in accordance with the policy described in the Instructions for Authors (www.plantphysiol.org) is: Takashi Hashimoto (hasimoto@bs.naist.jp).

T.Ha. designed the experiments; J.H.W., T.K., S.A.B., R.S., and N.K. prepared materials and conducted experiments; T.K. and Y.S., respectively, wrote the mathematical models for MtCurv and BQuant; T.K., T.Hi., and Y.S. did statistical analyses; T.Ha., T.K., and D.B.S. interpreted the results; T.Ha. wrote the article with contributions from all authors.

www.plantphysiol.org/cgi/doi/10.1104/pp.19.00811

behaviors of both cells at the lobing interface must be coordinated precisely (Szymanski, 2014). During a subsequent phase of lateral diffuse growth, pavement cells follow an already established cell geometry to accentuate highly interdigitated shapes and generate alternating regions of protrusions and indentations (Zhang et al., 2011; Elsner et al., 2012; Armour et al., 2015). The functional significance of highly interdigitated cell shapes is not clear. They may be important for increasing adhesive strength between neighboring pavement cells (Jacques et al., 2014), to afford groups of neighboring cells in the epidermis a higher degree of plasticity with respect to heterogeneous growth rates (Szymanski, 2014), and to provide mechanical stability to the outer periclinal (parallel to the leaf surface) wall of the epidermis (Glover, 2000). This cell face that lacks neighbors is subjected to high mechanical stress produced by turgor pressure (Szymanski, 2014; Eng and Sampathkumar, 2018; Kierzkowski and Routier-Kierzkowska, 2019; Sapala et al., 2019).

Pharmacological intervention studies during leaf development indicate that the microtubule cytoskeleton is involved in lobe morphogenesis (Panteris and Galatis, 2005; Akita et al., 2015); however, the precise roles of microtubules during lobe initiation and outgrowth are not understood (Panteris et al., 1994; Belteton et al., 2018). Certainly there are observable patterns of microtubules in static images of pavement cells. In the leaf epidermal cells of several plant species, bundles of cortical microtubules are observed underneath the straight anticlinal walls of young pavement cells before lobe initiation (Panteris and Galatis, 2005). Subsets of these anticlinal microtubules appear to extend to the outer periclinal wall, generating a fan-like microtubule array at the junction of the anticlinal–periclinal transfacial wall at the convex side of subsets of lobes (Panteris and Galatis, 2005; Zhang et al., 2011; Armour et al., 2015; Belteton et al., 2018). These microtubules were proposed to locally restrict growth (Fu et al., 2005) or generate a local thickening of the cell wall that would restrict growth and promote lobe formation. Thickened cell wall pads are certainly present at the interface of the outer and inner periclinal walls of lobed cells (Panteris and Galatis, 2005). However, in Arabidopsis pavement cells at the stage of lobe initiation, there is no clear correlation between the presence of microtubule bundles and cell wall thickness (Belteton et al., 2018). It has been proposed that a subpopulation of aligned microtubules in the outer periclinal cell surface of one cell generates a patch of anisotropic strain and drives lobe initiation (Szymanski, 2014). Similar mechanisms may also promote lobe outgrowth (Panteris and Galatis, 2005). In one study, lobe initiation and microtubule organization were simultaneously monitored at 1 DAG and 7 h later, anticlinal microtubules were stated to be enriched near the anticlinal walls that subsequently developed into lobes (Armour et al., 2015). A subsequent time-lapsed analysis that accurately monitored cell boundary shape with a plasma membrane marker showed that lobe initiation is detectable as a tiny and localized ~200-nm deflection that appears on the time scale of hours (Belteton et al., 2018). Statistical analyses of cell boundary and microtubule signals failed to detect stable anticlinal microtubules or microtubule patterns that clearly predicted lobe initiation. Therefore, the spatial and temporal scales at which microtubules affect lobe formation are not known. Further, numerous lobe initiation mechanisms have been proposed that could involve specialized microtubule arrays, cell geometry, cell wall stress patterns, and biomechanical heterogeneities in the cellulose and matrix polysaccharides (Szymanski, 2014; Belteton et al., 2018; Majda et al., 2017; Bidhendi et al., 2019).

The subcellular growth patterns associated with lobe initiation are not known. In lobed cells, the growth of periclinal walls is heterogeneous and anisotropic, with maximal extension usually occurring in the direction along the lobe axis (Elsner et al., 2018). The microtubule arrangement in pavement cells is also highly variable in space and time. During this lobe maturing stage, stable cortical microtubules are often observed to align parallel in indented regions on the outer periclinal face of the cell (Fu et al., 2005; Zhang et al., 2011; Sampathkumar et al., 2014a). This radial pattern of microtubules is likely to generate a similar local pattern of organized microfibrils that could promote anisotropic strain parallel to the lobed region and promote asymmetric lobe outgrowth (Panteris and Galatis, 2005; Szymanski, 2014). Feedback control between cell shape and the microtubule systems of lobed cells is possible, as the splayed microtubule arrangement subsets of cell indentations is qualitatively mirrored by the simulated pattern of the maximal tensile stress direction that is influenced by local curvature and cell geometry (Sampathkumar et al., 2014a). Such a pattern is expected, as microtubules are known to align to the direction of maximal physical stresses in the wall (Sampathkumar et al., 2014b; Robinson and Kuhlemeier, 2018; Verger et al., 2018). The role of actin during lobe formation is less clear. The mild effects of cytochalasin D, an actin-filament-depolymerization drug, and several actin-related mutants on pavement cell morphogenesis suggest that actin filaments participate in the further outgrowth of lobes, but not in lobe initiation, during a later phase of isotropic cell expansion (Panteris and Galatis, 2005; Armour et al., 2015).

Previously, we purified and identified dozens of microtubule-associated proteins (MAPs) from Arabidopsis cell suspension cultures (Hamada et al., 2013). BASIC PRO-RICH PROTEIN1 (BPP1) is one of the MAPs identified in that study, and constitutes a seven-member BPP family in Arabidopsis. The basic Pro-rich domain in BPP1, which is devoid of acidic amino acids, is necessary and sufficient for microtubule binding when ectopically expressed in onion (*Allium cepa*) epidermal cells (Hamada et al., 2013). Overexpression of *BPP1* in Arabidopsis plants inhibits microtubule depolymerization in the presence of microtubule-depolymerization drugs, and causes right-handed

helical growth and ectopic outgrowth of epidermal cells in elongating tissues, whereas *bpp1* single knockout mutants are indistinguishable from wild-type plants in growth and morphology (Hamada et al., 2013).

In this study, we generated multiple *bpp* mutants that exhibited severe phenotypes in lobe morphogenesis. These *bpp* mutants not only offer excellent opportunities to assess the functional roles of characteristic microtubule structures that have been implicated in lobe initiation and outgrowth but also enable us to test whether the mutants' three-dimensional cell shapes conform to the computationally modeled biomechanics.

RESULTS

Predominantly Expressed BPP-Family MAPs in Arabidopsis Plants

The Arabidopsis genome contains seven *BPP* genes, *BPP1* to *BPP7*. These *BPP* genes encode proteins with highly basic regions (pI values of 12.1–13.4). A search for BPP homologs in sequenced plant genomes (Phytozome v12.1; https://phytozome.jgi.doe.gov/pz/portal.html) revealed that *BPP* genes are absent in algae, exist in small numbers in mosses (two tandemly duplicated genes in *Physcomitrella patens*), and are considerably expanded in vascular plants (Supplemental Fig. S1; Supplemental Table S1).

We first examined whether the seven Arabidopsis BPP proteins could associate with microtubules in vivo. GFP-BPP1 and GFP-BPP2 fusion proteins have been previously shown to label cortical microtubules when transiently expressed in onion epidermal cells (Hamada et al., 2013). In our constructs, GFP was fused to the N terminus of each BPP, and the combination was expressed under the control of the *UBIQUITIN10* promoter in an Arabidopsis microtubule-marker line expressing the mCherry reporter fused to β-tubulin 6 (mCherry-TUB6; Fig. 1A; Supplemental Fig. S2). GFP-BPP5 was expressed under the control of its own regulatory elements. When we examined the epidermal cells of the primary roots, we found that all seven BPP-GFP fusions were localized on cortical microtubules, which were colabeled with mCherry-TUB6. Cortical microtubules were labeled uniformly by BPP-GFPs; no punctate or biased microtubule labeling was observed. These results indicate that all seven Arabidopsis BPPs are MAPs that bind the microtubule lattice.

We next studied the expression patterns of Arabidopsis *BPP* genes. We first fused the 5′-upstream region (~2.6 kb) of each *BPP* gene with the β-glucuronidase (GUS) gene, and stably expressed each one in Arabidopsis plants. Of the seven BPP promoters tested, the *BPP1*, *BPP2*, and *BPP5* promoters drove considerable GUS expression in many tissues, including cotyledons, rosette leaves, cauline leaves, roots, stems, flowers, stamens, siliques, and pollen grains (Fig. 1B; Supplemental Fig. S3). Cotyledons and leaves of very young seedlings were stained strongly. In developing

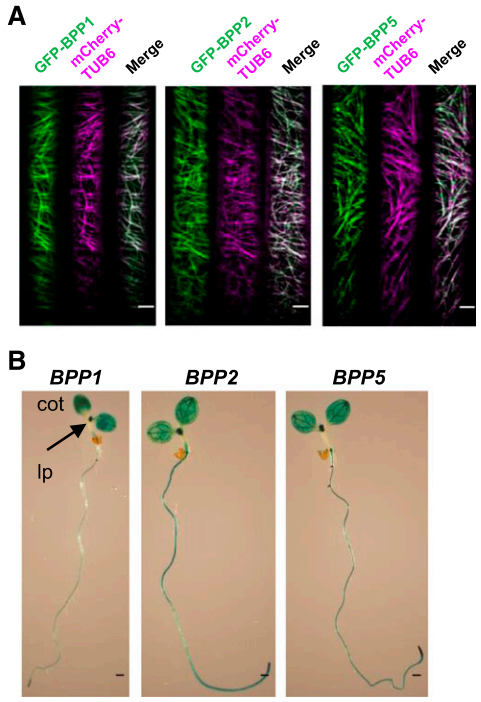

Figure 1. BPP1, BPP2, and BPP5 bind microtubules in vivo, and are expressed in cotyledons and leaf primordia. A, Subcellular localization of GFP-BPPs. In the mCherry-TUB6 expressing plants, GFP-BPP1 and GFP-BPP2 were expressed constitutively under the *UBIQUITIN10* promoter, whereas GFP-BPP5 was expressed by its own genomic regulatory elements. Confocal images of the epidermal cells of 8-d–old seedlings are shown. Scale bars = 5 μm. B, Expression patterns of *BPP* genes. GUS expression was driven by the *BPP* promoters. Three-d–old seedlings were analyzed. Cot, cotyledon; lp, leaf primordium. Scale bars = 5 mm.

leaves, GUS expression gradients from the leaf base to the tip were observed. We detected weak GUS staining in *BPP4*-, *BPP6*-, and *BPP7*-promoter lines in the leaf and root primordia, leaf vasculature, and inflorescent stem (*BPP4*-promoter lines), in vasculature and pollen grains (*BPP6*-promoter lines), and in pollen grains (*BPP7*-promoter lines). We did not observe GUS expression in Arabidopsis transgenic lines expressing GUS under the *BPP3* promoter used.

In support of the promoter-GUS expression analysis, reverse transcription-PCR analysis detected *BPP1*, *BPP2*, and *BPP5* transcripts in the tissues of Arabidopsis plants where positive GUS staining was observed, whereas other *BPP* transcripts were sporadically detected in several tissues (Supplemental Fig. S4). The Arabidopsis database on transcript abundance (Genevestigator; https://genevestigator.com/gv/) shows that *BPP1*, *BPP2*, and *BPP5* transcripts are most abundant among the seven *BPP* transcripts in all plant organs at several developmental stages (Supplemental Fig. S5). These expression results indicate that *BPP1*, *BPP2*, and *BPP5* are the major *BPP* genes expressed in many Arabidopsis tissues throughout plant development.

Mutations in *BPP1*, *BPP2*, and *BPP5* Affect Anisotropic Growth

To investigate the functions of BPPs, we identified Arabidopsis knock-out mutants caused by T-DNA insertion in the exon regions of *BPP1*, *BPP2*, or *BPP5* (Supplemental Fig. S6). Reverse transcription-PCR analysis showed that no corresponding *BPP* transcripts were present in these mutants, confirming that they are null alleles (Supplemental Fig. S7). In this study, we used the *bpp1-4*, *bpp2-5*, and *bpp5-1* null alleles for further analysis, and generated double and triple mutants with these alleles.

We then analyzed the morphology and growth of various single and multiple *bpp* mutants (Supplemental Fig. S8). At the seedling stage, primary roots of *bpp1*, *bpp2*, and their multiple mutants were shorter than those of wild-type plants. Elongation of petioles and leaf blades was impaired, particularly in *bpp1-4*;*bpp5-1* (hereafter referred to as "*bpp15*") and *bpp1-4*;*bpp2-5*;*bpp5-1* (hereafter referred to as "*bpp125*") plants, which resulted in a dumpy appearance of true leaves. At the reproductive stages, plant stature was somewhat smaller in *bpp5* and in the multiple mutants, than in the wild type. Siliques were shorter in *bpp1*, *bpp5*, and their multiple mutants. We also found that these growth phenotypes of *bpp15* and *bpp125* were complemented by introducing the genomic fragment of GFP-fused *BPP1* or GFP-fused *BPP5* (dubbed here "*GFP-gBPP1*" and "*GFP-gBPP5*"; Supplemental Fig. S9, A and B). These results indicate that *BPP1* and *BPP5* regulate plant anisotropic growth and function redundantly, whereas the function of *BPP2* is weakly redundant with *BPP1* and *BPP5* in some tissues.

Lobe Growth Is Severely Impaired in *bpp* Mutants

The *bpp* mutants presented a useful opportunity to analyze the function of a known MAP in pavement cell morphogenesis in detail. At 1 DAG, the adaxial epidermis of just-unfurled wild-type cotyledons contained small polyhedral pavement cells with subtle local undulations on the anticlinal walls. By 3 DAG, the pavement cells became more complex in shape with multiple lobes (Fig. 2A). We found that the cotyledon pavement cells of *bpp15* and *bpp125* mutants have much less complex shape and highly underdeveloped interdigitation (Fig. 2A). Expression of *GFP-gBPP1* or *GFP-gBPP5* in these mutants restored the cell shape complexity to wild-type levels (Supplemental Fig. S9C), indicating that *BPP1* and *BPP5* are largely responsible for the defective morphology of pavement cells.

We next analyzed the effects of *bpp* mutations on lobe initiation and outgrowth. The ImageJ-based shape quantification tool, PaCeQuant (Möller et al., 2017), was used to segment individual cells from the images and objectively quantify cell shape parameters in populations of wild-type and *bpp125* mutant cells. First, global cell shape features were analyzed. Average cell area increased steadily from 1 DAG, with the period of fastest cellular growth observed between 2 and 3 DAG when cell areas increased 3.8–3.9 times (Fig. 2B). The fastest growth period in pavement cells of wild-type Arabidopsis cotyledons was previously found between 1 and 2 DAG (Armour et al., 2015); the difference might be attributable to different growth conditions. The *bpp* mutant cells had somewhat larger cell area compared to wild-type cells of the corresponding growth stage after 2 DAG. The circularity, an index of cell roundness, continued to decrease from 1 to 5 DAG in wild-type cells, while the index did not decrease and remained at high values in the mutant cells, indicating the mutant cell shape does not become more complex during development (Fig. 2C). The solidity is another index of cell complexity, which calculates the ratio of the cell area and the area of the convex hull, and showed similar results with those of the circularity in wild-type and mutant cells (Fig. 2D).

Next, we measured several parameters specifically related to lobes. PaCeQuant detected ~5 incipient lobes in both wild-type and *bpp125* pavement cells at 1 DAG; the lobe numbers slowly increased at 2, 3, and 5 DAG (Fig. 2E). The lobe numbers were not statistically different between wild-type cells and the mutant cells at each stages of lobe development. When the same dataset was analyzed by the convex hull-based algorithm LobeFinder (Wu et al., 2016), the LobeFinder counts of lobe numbers increased over 5 d for both genotypes (Fig. 2F). The *bpp125* cells showed marginally significantly lower numbers of lobes at 3 DAG and 5 DAG compared to wild-type cells. The data inconsistency between the two methods may be because of their different sensitivities to detect consecutive small wall undulations (as seen in the 3/5 DAG mutant cells) as single or multiple lobes. It is also possible that a subset of small features in *bpp* cells that are detected by LobeFinder at early time points disappear as the cell expands for days in the absence of persistent lobe outgrowth. During the initial wave of lobe initiation at 1 and 2 DAG, however, LobeFinder detected no differences in lobe numbers between the two genotypes. These results indicate that the *bpp* mutations do not have an obvious effect on lobe initiation.

Two different types of lobes exist based on their location to 3-way cell wall junctions that form during cytokinesis. Type-I lobes are formed during cellular expansion at the interface of two cells between two three-way junctions, whereas type-II lobes are located at three-way cell wall junctions (Wu et al., 2016). We extracted type-I lobes automatically from the lobe populations according to Möller et al. (2017; Supplemental Fig. S10). Average height of type-I lobes did not markedly increase between 1 and 2 DAG in both wild-type and the *bpp125* mutant cells, and did not significantly differ between the two genotypes at 1 and 2 DAG (Fig. 2G). Lobe height, however, increased 5.2 times in wild-type cells between 2 and 3 DAG, when the cell size increased rapidly in our samples (Fig. 2B). In the mutant cells, the increase in

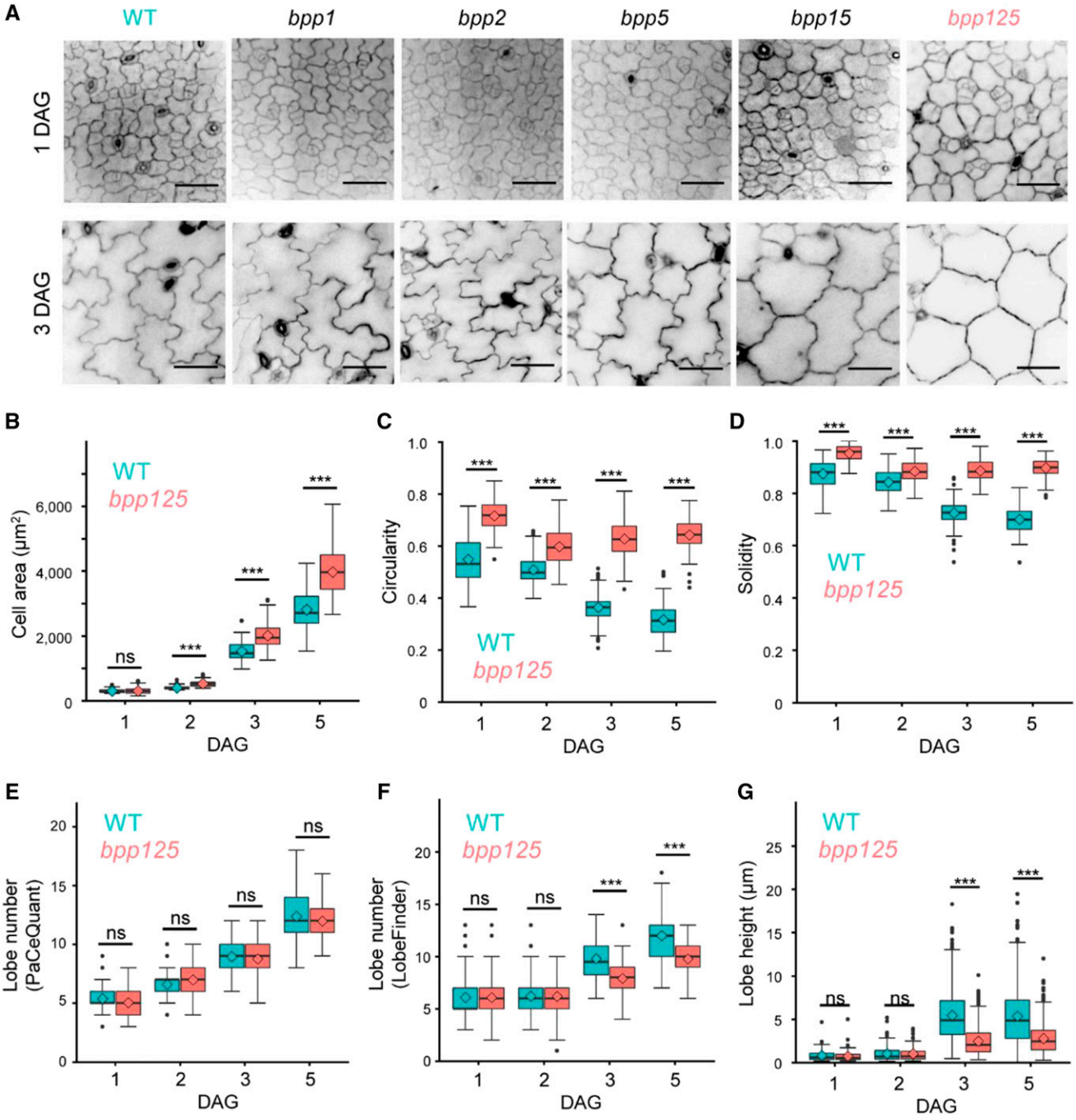

Figure 2. Incipient lobes in *bpp125* mutant cells do not grow. A, Confocal images of pavement cells of wild-type (WT), *bpp1*, *bpp2*, *bpp5*, *bpp15*, and *bpp125* cotyledons at 1 and 3 DAG. Scale bars = 10 μm. B–G, Cell shape parameters in wild-type and *bpp125* cells at 1 DAG, 2 DAG, 3 DAG, and 5 DAG. B, Cell area. C, Cell circularity. D, Cell solidity. E, Lobe number estimated by PaCeQuant. F, Lobe number estimated by LobeFinder. G, Lobe height. Asterisks indicate significant difference between the paired genotypes by Student's *t*-test (***$P < 0.001$). $n = 90$ cells from three cotyledons for each genotype and each time point. ns, not significant.

lobe height was modest (2.4-fold) between 2 and 3 DAG. Between 3 and 5 DAG, increase in average lobe height slowed down or ceased in both genotypes. When the ratio of lobe height to lobe equator width was analyzed, similar results were obtained (Supplemental Fig. S11). We thus conclude that the *BPP* genes are essential for anisotropic lobe growth during rapid cell expansion.

Mutant Pavement Cells Bulge Outward as They Enlarge

We noted that the outer periclinal cell wall of the mutant pavement cells bulged outward on both the inner and outer periclinal sides of the cells, which became increasingly apparent as the cell enlarged (Fig. 3A). To reliably quantify the maximal cell height of highly interdigitated complex cells, we measured the cell height at the center of the largest empty circle (LEC). The degree of tensile stress in the cell wall is related to cell geometry (Jordan and Dumais, 2010), and with all other parameters being equal, increases with cell diameter (Yanagisawa et al., 2015). A finite element method simulation proposes that the maximal stress in the outer cell wall of epidermal cells is approximated by the size of LEC that can fit into the cell contour (Sapala et al., 2018). The maximal stress point in the outer cell wall is calculated to be at the center of LEC (Sapala et al., 2018), which is expected to deform the cell wall most, giving rise to the maximal height of the pavement cell.

We measured both the cell area and the LEC area in wild-type and *bpp125* cotyledon pavement cells at 1, 2, 3, 5, and 8 DAG. The LEC area steadily increased as the cells enlarged (Fig. 3B). In wild-type cells, the magnitude of the LEC area increase was limited because of the interdigitated cell shapes (linear regression analysis; $y = 0.177x + 112$, where y is the LEC area and x is the cell area; $R^2 = 0.87$), whereas *bpp125* cells showed steady increases in LEC area as they grew ($y = 0.629x - 143$; $R^2 = 0.94$). Larger LEC area would predict that the outer periclinal wall of *bpp* pavement cells would experience increased tensile stress.

The height of the pavement cells was largest at the center of the LEC (Fig. 3A). The maximal cell height at the LEC center was 1.5 times and 1.7 times larger in the *bpp125* cells than in wild-type cells at 3 and 5 DAG (Fig. 3C), indicating that the periclinal cell walls yield to the increased mechanical stress. When the maximal heights (y-axis) of both wild-type and *bpp125* cells at 3, 5, and 8 DAG were plotted against the radii of the LEC (x-axis), a significantly high linear correlation was observed, regardless of genotypes ($y = 1.41x - 1.22$; $R^2 = 0.97$; Fig. 3D).

Subcellular Localization of BPP1 during Lobe Formation

To examine whether BPPs are targeted to particular subsets of microtubule populations during lobe formation, we analyzed the subcellular localization of functional GFP-BPP1 expressed under the control of the native regulatory elements in the *bpp125* background. At 1 DAG when distinct lobe morphology had yet to be apparent, anticlinal microtubules and periclinal radiating microtubules at the cell cortex regions were

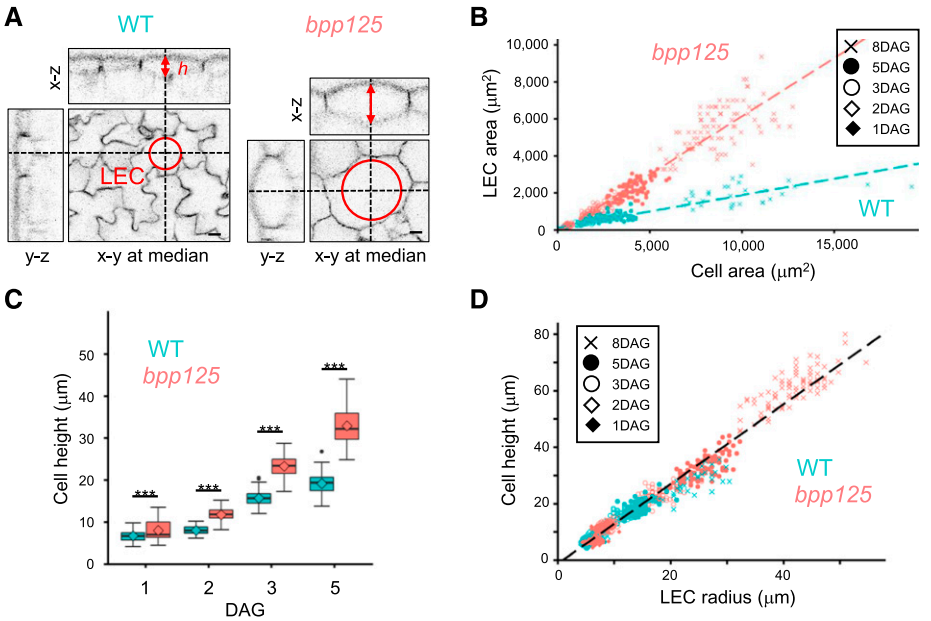

Figure 3. Periclinal walls of *bpp125* cells bulge out as they enlarge. A, Confocal images of wild-type (WT) and *bpp125* cotyledon pavement cells at 8 DAG. Images of pavement cells at the *x*–*y* focal plane near the median region are shown in the center, accompanied by orthogonal scanning views of the *y*–*z* and *x*–*z* planes on the right and above, respectively. LECs (red circle) are shown in representative cells. The greatest height of pavement cells was measured at the center of the LEC (crossing point of the two dotted lines). Scale bars = 20 μm. B, Relationship between cell area and LEC size in wild-type and *bpp125* cotyledon pavement cells at 1, 2, 3, 5, and 8 DAG. C, Box plots of cell height at 1, 2, 3, and 5 DAG. Asterisks indicate significant difference between the paired genotypes by Student's *t*-test (***$P < 0.001$). D, Relationship between the LEC radius and the cell height for individual cells of wild type and *bpp125* at 1, 2, 3, 5, and 8 DAG. $n = 90$ cells from three cotyledons for each genotype and each time point, except wild-type cells at 8 DAG with $n = 30$ from three cotyledons.

strongly labeled (Fig. 4, A and B). To track the subcellular localization of GFP-BPP1 in relation to microtubules, we introduced an mCherry-TUB6 microtubule marker into a GFP-BPP1-expressing line to label BPP1 and cortical microtubules simultaneously. BPP1 and microtubules colocalized extensively on anticlinal microtubule bundles and periclinal radiating microtubule arrays at the early phase of pavement cell morphogenesis (Fig. 4, C and D).

Periclinal Microtubule Arrays during Lobe Formation

Next we analyzed microtubule organization in Arabidopsis plants expressing the GFP-TUB6 microtubule marker at 2 DAG, when the average lobe size was indistinguishable between wild-type and mutant cells (see Fig. 2G). In wild-type pavement cells, periclinal cortical microtubules were often enriched at the convex side of the developing lobes and splayed out from the convex region, whereas in the *bpp125* cells cortical microtubules generally aligned parallel to the anticlinal wall and distinct microtubule enrichment on the convex side was not apparent (Fig. 5A). We processed microtubule images of 2 DAG pavement cells into skeletons using the cortical occupancy method (Higaki et al., 2010) and quantified the regions of interest of the two opposing cortical regions for the skeletonized microtubule signals (Belteton et al., 2018). The cortical density of periclinal microtubules on the convex and concave cell surfaces does not differ before the lobe is detectable using a plasma membrane marker (Belteton et al., 2018). However, in lobed cells the cortical density of periclinal microtubules in wild-type cells was significantly higher at the convex side than at the concave side, whereas the microtubule density was indistinguishable between the two sides of the anticlinal wall undulation in the *bpp125* mutant cells (Fig. 5B). In an independent experiment, we also measured microtubule density by counting the number of cortical microtubules that crossed a defined line at the convex or concave sides of incipient lobes (Fig. 5C). Periclinal microtubules were significantly enriched at the convex side of young lobes in wild-type cells, whereas there was no significant enrichment of microtubules near one side of the forming lobes in the *bpp125* mutant cells. The protruding concave regions of pavement cells are not devoid of cortical microtubules as they are frequently detected in single cell labeling experiments (Qiu et al., 2002; Zhang et al., 2011).

To objectively score the presence or absence of fan-like periclinal arrays with respect to lobe geometry, we developed an image analysis protocol, MtCurv, that evaluates the microtubule status in relation to the curvature of the nearby anticlinal wall (Fig. 6A; Supplemental Fig. S12; see "Materials and Methods" for detailed description). A cell contour was first extracted from a median cross-section image of the pavement cell and was shrunk evenly by 5 pixels (1.09 μm) to give a loop of interest (LOI; Fig. 6A). Circles were generated to match the local curvature of the LOI and were used to span the perimeter at 1-pixel intervals; a circumscribed circle indicates the convex side of a lobe, whereas an inscribed circle shows the concave side (Fig. 6A). The circle radius and the direction to the circle center, respectively, define the degree and orientation of the local cell curvature. Images of cortical microtubules were assessed for relative signal intensity of GFP-TUB6 (with the highest value of 1.0 in each cell) at 1-pixel intervals on the LOI. Several threshold values were tested to eliminate background fluorescence (Supplemental Fig. S13). With the threshold value of

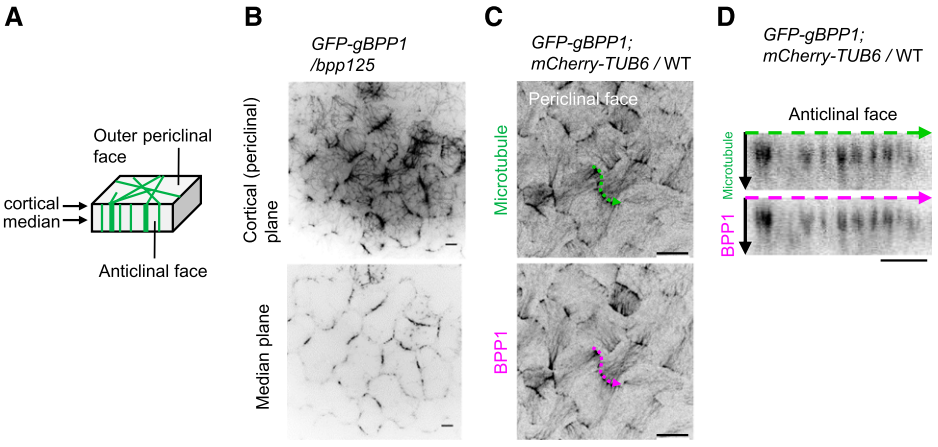

Figure 4. BPP1 labels radiating microtubule arrays on the outer periclinal wall and microtubule bundles on the anticlinal wall. A, Schematic of cell face nomenclature. B, Subcellular localization of GFP-BPP1 expressed under the control of its own regulatory elements in the *bpp125* background. Cotyledon pavement cells at 1 DAG were imaged at the cortical (periclinal) plane and at the median plane. Scale bars = 5 μm. C, Confocal images of mCherry-TUB (labeling microtubules) and GFP-BPP1, which was expressed under genomic regulatory elements, in cotyledon epidermal cells at 1 DAG. Cortical microtubules underneath the outer periclinal wall are shown. Scale bars = 20 μm. D, Anticlinal microtubules were scanned toward the *z* plane (solid arrow) along the dashed lines in (C). Scale bar = 10 μm. WT = wild type.

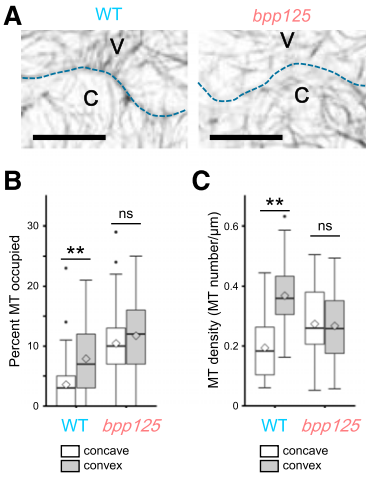

Figure 5. Periclinal cortical microtubules are not enriched at the convex side of the incipient lobes in *bpp125* cells. Cotyledon pavement cells of wild-type (WT) and *bpp* mutant seedlings expressing GFP-TUB6 were analyzed at 2 DAG. A, Live-cell images of pavement cells. Anticlinal walls are indicated by dotted blue lines. Microtubule density at the opposing concave (C) and convex (V) sides were analyzed. Scale bars = 10 μm. B, Box plot of microtubule occupancy. Ten and eight undulation regions were analyzed for 10 cells of wild type and *bpp125*, respectively. For each region of interest, microtubule density was measured at four to nine time points. C, Microtubule density per unit length shows that enrichment of periclinal microtubules at the convex side only occurs in wild-type cells. Asterisks indicate significant difference between the paired cell regions and paired cell lines by Student's *t*-test (*$P < 0.05$ and **$P < 0.01$, respectively). Thirty undulation regions from 10 cells were analyzed per genotype. MT, microtubule; ns, not significant.

0.3, microtubule signals in 2-DAG wild-type cells (6 cells; n = 1,114 sampling points) were distributed more toward the convex side, whereas those in the *bpp* cells (6 cells; n = 1,355 points) did not show significantly biased distribution toward either side of the lobes (Fig. 6B), indicating that the microtubule density is higher on the convex side than on the concave side in the wild-type cells, but not in the mutant cells. These results are consistent with those of the more geometrically subjective analyses shown in Figure 5. Microtubule signals above the threshold value of 0.3 were therefore used for subsequent analyses.

To further characterize the microtubule status, OrientationJ, an ImageJ plug-in for local angular density distribution of fibers (Rezakhaniha et al., 2012), was used to calculate the microtubule orientation with respect to the local cell curvature and the coherency of microtubules at that position (Supplemental Fig. S14). Orientation and coherency are bound between 0 and 1. An orientation value of 1 indicates a microtubule oriented toward the direction of the normal vector of the curvature circle (which is perpendicular to the neighboring anticlinal wall), whereas a microtubule with an orientation value of 0 is arranged perpendicular to the vector. Coherency values of 1 and 0 indicate perfectly aligned microtubules and randomly oriented microtubules, respectively.

Figure 6C shows the distributions of coherency values obtained from 2 DAG pavement cells of wild-type and the *bpp125* mutant cells. Mutant microtubules (0.406 ± 0.182, mean ± SD) were more coherently aligned than wild-type microtubules (0.362 ± 0.160; $P < 0.001$; Welch's two sample *t*-test). We analyzed the dataset in two ways. First, all the microtubules were subjected to the analysis. Second, to focus on microtubules that were more aligned and to eliminate discordant microtubules, we selected microtubules that possessed coherency values higher than 0.5. Distributions of orientation angles relative to the nearby anticlinal wall (Fig. 6D) in the two microtubule populations are shown in Figure 6E. Wild-type microtubules and mutant microtubules differed significantly ($P < 0.05$ in all microtubules and $P < 0.001$ in microtubules with >0.5 coherency; Welch's two sample *t*-test). In the high coherency subpopulation, wild-type microtubules were oriented broadly over all directions (0.433 ± 0.358, mean ± SD; n = 217), while the orientations of mutant microtubules were considerably biased toward the direction parallel to the wall (0.309 ± 0.335; n = 434; Fig. 6D).

We classified microtubules into two orientation groups: "splayed" microtubules that fan out from the cell periphery inward with dominant orientation angles of between 45° and 135° relative to the wall, and "parallel" microtubules that are more aligned with the wall (with angles of between 0° and 45°, and between 135° and 180°; Fig. 6D). We next examined how these microtubule groups are located with respect to the curvature of young lobes. As shown in Figure 6F, both microtubule groups in wild-type cells were located preferentially in the convex regions. In the high coherency microtubule subpopulation, the splayed microtubules with orientation values of >0.5 showed a more pronounced convex-side bias than those in the parallel group (0.035 ± 0.032 versus 0.020 ± 0.035, mean ± SD; $P < 0.001$; Welch's two sample *t*-test). Microtubules in the mutant cells, on the other hand, were not enriched on either the convex or concave side, but were located primarily on the flat regions of the anticlinal wall. For both microtubule groups in either microtubule population, distributions over the wall curvatures were significantly different between the wild-type and *bpp125* cells ($P < 0.001$; Welch's two sample *t*-test). Figure 6G shows examples where microtubules classified as the splayed or parallel groups were located on the LOI. In the wild-type cells, these microtubules are enriched in the convex regions of the lobes. Not all convex regions had the splayed microtubules. While some convex regions are enriched with the splayed microtubules, other convex regions are dominated by the parallel microtubules or are mixed with both types of the arrays. By contrast, in the mutant cells, they mostly occurred near the relatively flat regions of the anticlinal wall.

We also analyzed the local abundance of fan-like microtubules by defining a splayed microtubule array index as an integrated value obtained by multiplying values of coherency and orientation of each

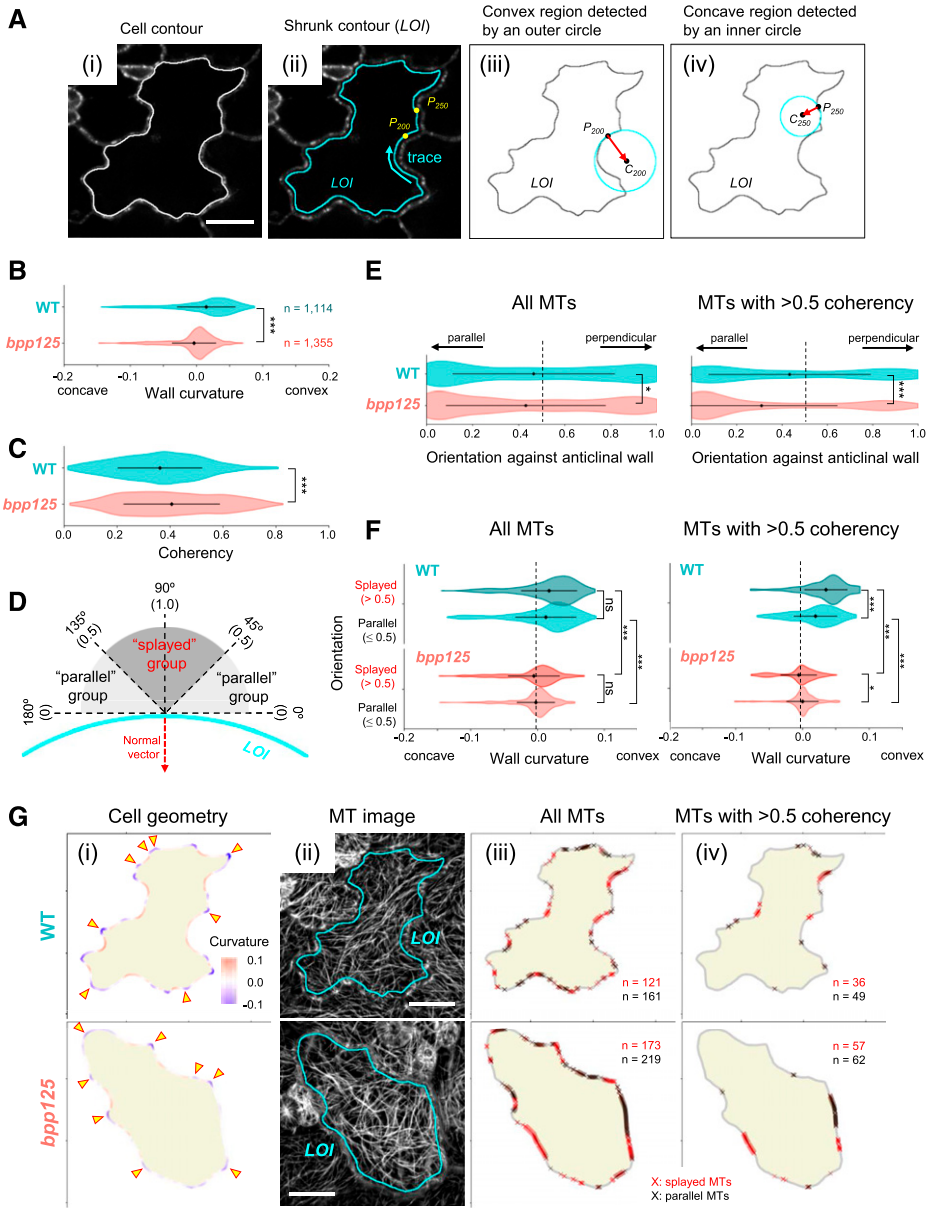

Figure 6. Periclinal microtubules do not fan out from the convex side of the incipient lobes in *bpp125* cells. A, MtCurv assigns individual cell peripheral positions with regard to the geometry of the adjacent anticlinal walls. First, a cell contour was extracted from the median cross section of *z*-stacked microtubule images (i), and a smaller cell contour image (LOI) was generated by shrinking the original contour inward by five pixels (ii). The LOI was then traced by fitting a circle of an appropriate size to the local curvature. Circles placed outside (iii) and inside (iv) the LOI, respectively, indicate the convex and concave regions of a cell. The circle radius and the direction to the circle center (red arrow), respectively, define the degree and orientation of the local cell curvature. B, Distributions of microtubule signals over the cell curvature in wild-type (WT) and *bpp125* cells at 2 DAG. Plus and minus values, respectively, indicate the convex and concave sides, while the value zero shows a flat wall region. C, Distributions of the coherency values. D, Schematic diagram of the "splayed" microtubule group (orientation values > 0.5) and the "parallel" microtubule group (orientation values < 0.5) with respect to the local curvature of the adjacent anticlinal wall. Values of 1.0 and 0, respectively, indicate that microtubules are oriented perpendicular (90°) and parallel (0° and 180°) to the tangent line of the anticlinal wall. E, Relative orientations with respect to the adjacent anticlinal walls. Microtubule subpopulations with coherency values > 0.5 are also analyzed on the right. F, Distributions of the "splayed" microtubules and the "parallel" microtubules with respect to the local wall curvature. All microtubules and microtubules with >0.5 coherency values were analyzed separately. G, In (i), the convex and concave regions are respectively indicated by red and purple, while the three-way cell junctions corresponding to the type-II lobes are indicated with arrowheads. Note that many concave regions with high negative curvature values correspond to type-II lobes. In (ii), images of cortical microtubules are shown together with the LOIs. In the right two columns, microtubules of the splayed group (red "X" symbols) and the parallel group (black "X" symbols) are mapped on the LOI. All microtubules (iii) and microtubules with >0.5 coherency values (iv) were analyzed and shown separately. Welch's two

microtubule (Supplemental Fig. S14). Well-aligned and perpendicularly oriented microtubules (with respect to the nearby anticlinal walls) scored high values in this analysis. Microtubules with high splayed microtubule index values were then plotted on the local wall curvature. This alternative method resulted in the microtubule distribution patterns in the wild-type and mutant cells that were highly similar to those obtained in the first method. Taken together, these results confirm, in a quantitative way, previous reports that the fan-like microtubules are enriched on the convex side of wild-type lobes (Panteris and Galatis, 2005; Zhang et al., 2011; Armour et al., 2015; Belteton et al., 2018; Bidhendi et al., 2019) and indicate that BPP proteins are required to establish this distinct microtubule array.

Anticlinal Microtubule Arrays during Lobe Formation

We also analyzed anticlinal microtubule distributions as a function of location and time. As reported in Belteton et al. (2018), the wild-type microtubule signals formed distinct peaks, and certain subregions of the anticlinal wall cortex were more likely to contain microtubule bundles, whereas others were more transient (Fig. 7A). In the *bpp* triple mutant cells, microtubule peaks were more broadly distributed along the anticlinal cortex, and regions of persistent microtubule signals were less distinct (Supplemental Fig. S15). Overall, microtubule densities during the whole observation period appeared to be lower in the mutant than in the wild type. To quantify the density and bundling status of crowded microtubules with various signal intensities, we developed a mathematical model for quantifying bundled filamentous structures, BQuant (see "Materials and Methods" for detailed description). We obtained optical sections that are roughly perpendicular to the vertically oriented microtubule bundles. In BQuant, fluorescence intensity distributions of scanned microtubule images are approximated by the sum of Gaussian functions, by fitting quantified data with Bayesian parameter constraints (Fig. 7, B and C). The distribution of signal intensities of individual peak heights was fitted by gamma distribution. By comparing individual small peaks and actual microtubule images, we set a cutoff value of 500 for each dataset to reduce background noise.

The distribution patterns of mathematically modeled microtubule peak heights indicated that wild-type cells contained significantly larger proportions of brighter microtubules than did the *bpp125* mutant cells (Fig. 7D). The distribution patterns of peak widths were not different between wild type and the mutant (Supplemental Fig. S16). Although various measurement factors may influence the signal intensities, bundled microtubules appear to be more abundant in wild-type cells than in the *bpp* mutant cells. When we quantified the number of corrected signal peaks, which would include both single and bundled microtubules per unit length, wild-type cells had three times the density of microtubules of the *bpp* mutant cells (Fig. 7E). The peak area, which may be considered a proxy for the total number of microtubules, implied that wild-type cells had 3.5-times more microtubules than the *bpp125* mutant cells (Fig. 7F).

Microtubule Organization in Mature Pavement Cells

When lobes have already formed and cells are expanding largely isotropically, periclinal cortical microtubules in wild-type cells tend to coalign toward the convex sides of many (but not all) opposing lobes (Fu et al., 2005; Zhang et al., 2011; Sampathkumar et al., 2014a). We used the program OrientationJ to assign values of orientation and coherency to cortical microtubules and expressed them as the angle and the length of a vector line (Fig. 8). Wild-type cotyledon pavement cells at 5 DAG had diverse microtubule localization patterns. In some instances, cortical microtubules were aligned toward the opposing indenting sides while in other locations microtubule alignment seemed random (Fig. 8). In the *bpp125* mutant cells of the corresponding developmental stage, cortical microtubules of many cells were organized in a concentric arrangement within LECs (Fig. 8; Supplemental Fig. S17). A concentric arrangement of cortical microtubules in the *bpp125* mutant cells follows the predicted mechanical stress pattern in the modeled lobe-less pavement cells that bulge at the cell center (Sapala et al., 2018), suggesting that microtubules align parallel to the mechanical stress in the bulged disk-shaped cells. Periclinal microtubules in the 5 DAG mutant cells were not enriched at, nor did they radiate from, the indenting anticlinal wall regions, as observed in the mutant cells at 2 DAG (Figs. 5 and 6).

DISCUSSION

Distinct organizations of cortical microtubules during lobe morphogenesis have been reported for many years in cotyledon pavement cells (see the introduction of this study), but genetic evidence was lacking to support their functional roles. The temperature-sensitive mutant of *MICROTUBULE-ORGANIZATION1* is a leading MAP candidate to strongly influence lobe formation (Kotzer and Wasteneys, 2006). Other previously reported Arabidopsis lobe mutants of MAPs were only modestly affected in lobe formation

Figure 6. (*Continued.*)
sample *t*-test was used to compare microtubule metrics between wild-type and the mutant cells (*$P < 0.05$ and ***$P < 0.001$). Scale bars = 20 μm. MT; microtubule; ns, not significant.

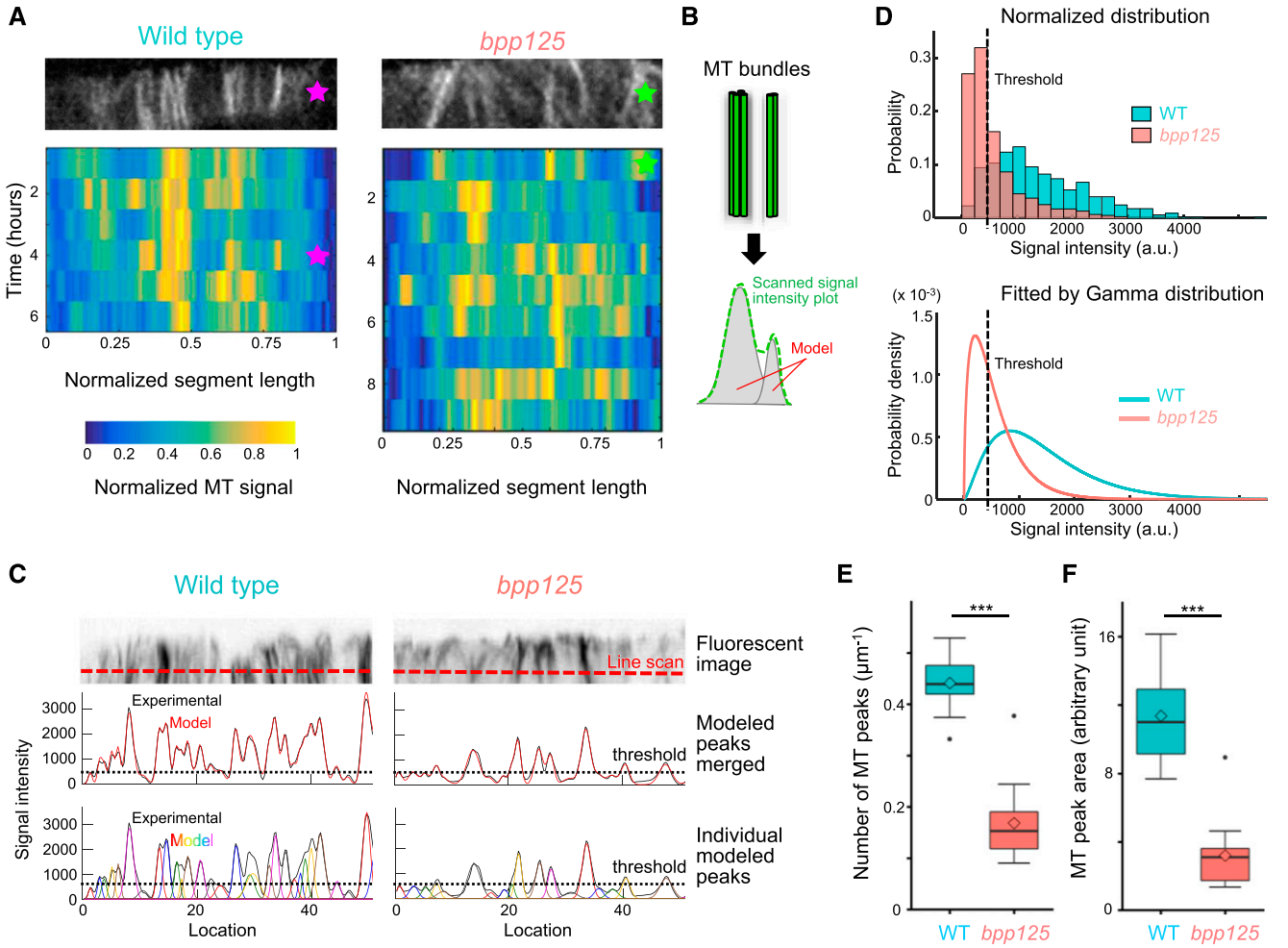

Figure 7. Anticlinal microtubule bundles are sparse in *bpp125* cells. A, Temporal stability of anticlinal microtubules at fixed locations. Heat maps of the normalized microtubule signals as a function of normalized segment length (*x*-axis) over time (*y*-axis) are shown. The magenta and green stars label the time points and locations of microtubule images of wild-type (WT) and *bpp125* cells shown above the maps. B, Microtubule bundles give increased fluorescence signals proportional to the composed microtubule numbers, and the distribution of a peak signal intensity can be approximated by Gaussian functions. Juxtaposed bundles give overlapping valley signals, which can be modeled by the sum of two Gaussian peak distributions. C, Fluorescence images of wild-type and *bpp* microtubules are line-scanned. Merged modeled peaks (red lines) faithfully reproduce experimentally observed signal intensity changes (black lines). Individual modeled peaks are shown in the lower. Setting a threshold cutoff value of 500 (dashed lines) excludes several small noise peaks from the analysis. D, Distribution of individual modeled peak heights in wild type (blue) and *bpp125* (red). Normalized distribution patterns (upper) were fitted by gamma distributions (lower). The threshold value is indicated by dashed lines. E and F, Box plots of bundle density (E) and microtubule density (F) in wild-type and *bpp* mutant cells. Asteriks indicate significant difference between the paired genotypes by Student's *t*-test (***$P < 0.001$). Nine cells were analyzed for each genotype. MT; microtubule.

(Ambrose et al., 2007; Kirik et al., 2007; Lin et al., 2013; Liang et al., 2018; Mitra et al., 2019). Decreased lobe morphogenesis in some mutants may be caused by the change in growth and organ shape from isotropic to elongated growth patterns (Lee et al., 2006; Sapala et al., 2018). In any of these mutant cells, microtubule organization has not been critically assessed with regard to initiation and growth of lobes. In this study, we identified novel Arabidopsis mutants that did not develop well-defined lobes and acquired a more polyhedral cell shapes in mature cotyledon pavement cells. To quantify microtubule phenotypes in pavement cells of an early lobe-outgrowth stage, two new methods were created. The strong and specific lobe phenotypes of the *bpp* mutant cells enabled us to determine functional requirements of distinct microtubule arrays on lobe initiation and growth.

Microtubule Defects and Lobe Morphogenesis in the *bpp* Mutant Cells

Previous studies showed that microtubule foci extending across the periclinal and anticlinal faces of a pavement cell were observed in Arabidopsis pavement

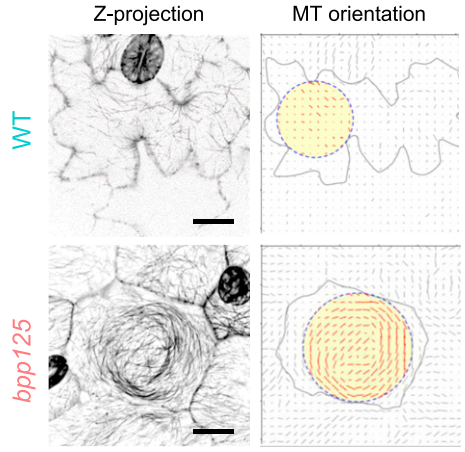

Figure 8. Periclinal cortical microtubules are organized in a concentric pattern in mature *bpp125* cells. Cotyledon pavement cells of wild-type and *bpp* mutant seedlings expressing GFP-TUB6 were analyzed at 5 DAG. Maximum-intensity projections along the *z*-axis (left) were image stacks covering 6.2 μm and 14.0 μm in depth of wild-type (WT) and *bpp125* pavement cells, respectively. On the right, local averaged orientations of microtubules are shown with vector lines. Longer lines indicate a higher degree of alignment. Cell contours and LECs are indicated. Scale bars = 20 μm. MT; microtubule

cells at 1 DAG (Armour et al., 2015), and are the basis for a growth restriction-based model for lobe initiation (Panteris and Galatis, 2005). On the other hand, quantitative time-lapse imaging analyses of microtubules and cell shape showed that locations of anticlinal microtubule bundles are not sufficient to predict the lobe initiation sites and that the density of periclinal microtubules in two adjacent cells are not necessarily enriched on the future convex side before lobe initiation (Belteton et al., 2018). In wild-type cotyledon pavement cells, the cortical density of periclinal microtubules increases at the convex side only after (Figs. 5 and 6), but not before (Belteton et al., 2018), lobe initiation. In this study, we found that anticlinal microtubule bundles are significantly less dense and associated periclinal fan-like microtubule arrays are not enriched in the convex side of incipient lobes in the *bpp* mutant cells, which nevertheless initiated the same number of lobes. Our results thus demonstrate that such characteristic periclinal arrays are dispensable for lobe initiation per se.

Cortical microtubules in the *bpp* cells do not become enriched on the periclinal face at the convex side of wavy anticlinal walls during early and late lobe morphogenesis stages. Because subsets of anticlinal microtubules are associated with a periclinal array (Panteris and Galatis, 2005; Zhang et al., 2011; Armour et al., 2015), significant reduction in the density of anticlinal microtubules in the mutant cells may be responsible for defects in the local enrichment of the transfacial microtubules that extend to the periclinal face. It has been proposed that this splaying periclinal microtubule array generates local anisotropic strain via targeted deposition of cellulose microfibrils and drives further anisotropic growth of initiated lobes (Panteris and Galatis, 2005; Szymanski, 2014). BPP1, BPP2, and BPP5 are strongly expressed at the lobe-formation stage of seedling development and are essential for the formation of the fan-like periclinal microtubule array, probably by way of their microtubule-stabilizing activities (Hamada et al., 2013). In the absence of this splayed array, a proposed feedback loop, in which cell-shape–derived stresses orient microtubules and cellulose microfibrils (Panteris and Galatis, 2005; Sampathkumar et al., 2014a), does not operate—thus preventing further outgrowth of local wall bending into distinct lobes during an extended phase of isotropic cell expansion.

Numerous models for lobe initiation have been proposed, and lobe initiation and outgrowth are likely to involve multiple mechanistically distinct processes (Majda et al., 2017; Belteton et al., 2018; Altartouri et al., 2019; Bidhendi et al., 2019; Fig. 9). Inhibitors and mutants in the microtubule pathway have effects on lobe initiation (Qiu et al., 2002; Fu et al., 2005; Panteris and Galatis, 2005; Kotzer and Wasteneys, 2006; Armour et al., 2015; Altartouri et al., 2019). The initial symmetry-breaking event that converts a straight anticlinal cell wall region to a wavy contour may involve some type of mechanical wall heterogeneities that is patterned by microtubules (Qiu et al., 2002; Panteris and Galatis, 2005; Szymanski, 2014). However, the exact roles of microtubules are not clear. In the *bpp125* mutant cells, anticlinal microtubules at this stage were significantly sparse but still present. It does not necessarily mean that the microtubule cytoskeleton is not involved in lobe initiation. Functional redundancy in the system may compensate for a loss of *BPP* activity. Alternatively, BPP-independent remaining microtubules beneath the anticlinal wall might have a role during lobe initiation. In the subsequent lobe outgrowth process, microtubule-mediated alignment of cellulose fibers on the periclinal convex side of an incipient lobe may create a local domain of anisotropic strain (Baskin, 2005) and promote local anisotropic growth. BPPs and the splayed microtubule arrays are essential for this process. The BPP-family MAPs and their mutants potentially provide important tools to dissect and analyze different morphogenetic events during lobe formation.

Interdigitated Cell Geometry Suppresses Excess Bulging of the Periclinal Walls

At the scale of individual cells (Sampathkumar et al., 2014a; Sapala et al., 2018; Bidhendi et al., 2019) and tissues (Sampathkumar et al., 2014b), shape changes are predicted to affect the spatial pattern of stresses. The considerable turgor pressure in plant epidermal cells (Forouzesh et al., 2013) induces tensile stress in the cell wall. As mechanical stress is predicted to be greater in larger cells, plant pavement cells withstand this mechanical problem by increasing the thickness of the outer periclinal wall (Kutschera, 2008), and perhaps by

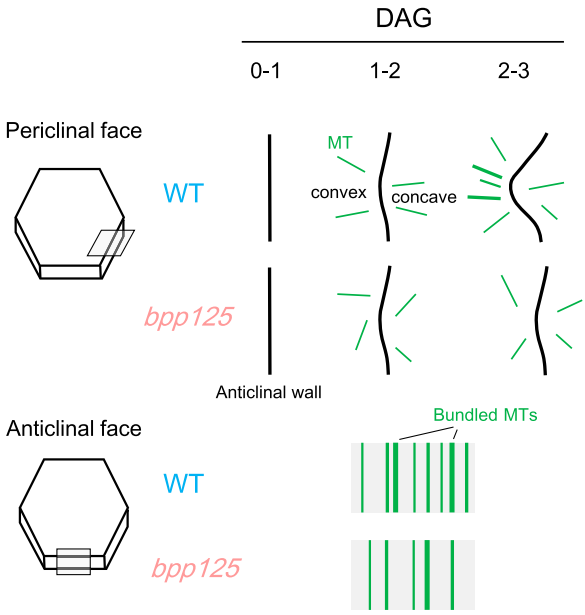

Figure 9. Two-step model of lobe initiation and outgrowth. Microtubules in the small rectangle regions of the hexagonal pavement cells (left) are shown on the right. By 2 DAG, small undulations are formed on the anticlinal wall in both wild-type (WT) and *bpp125* pavement cells. BPP-mediated microtubule (MT) arrays are not involved in this initial symmetry-breaking process. Incipient lobes grow after 2 DAG in wild-type cells where fan-like periclinal MTs and bundled anticlinal MT are organized on the convex side of the lobe. In the *bpp125* cells, anticlinal MT bundles are sparse and periclinal splayed arrays do not form, resulting in severe inhibition of lobe outgrowth.

reducing the cell size by cell division or by growing mostly anisotropically into long, thin cells, as seen in roots and stems (Sapala et al., 2018). In isotropically expanding pavement cells of cotyledons and leaves, lobe formation is proposed to effectively reduce mechanical stress in the cell wall (Sampathkumar et al., 2014a; Sapala et al., 2018).

Wall stress is proportional to the radius of the cell, and a finite element method simulation predicts that the maximal stress acting on pavement cells develops in the cell center and can be expressed by the size of the LEC (Sapala et al., 2018). Compared to wild-type cells, *bpp125* pavement cells during a lateral isotropic expansion phase (3 DAG to 8 DAG in this study) showed considerably larger LEC area for a given cell area, and bulged out, as shown by significantly increased cell height. The cell height of wild-type cells and *bpp* cells was highly proportional and linear to the radius of the LEC (the R^2 value of 0.97). The simulation of LEC proposed as a proxy for the maximal wall stress assumes mechanically homogeneous cell wall properties (Sapala et al., 2018). Although the composition of the cell wall is complex (Cosgrove, 2014), this assumption appears to hold at least on average, given the resolution of this study, for the periclinal walls of the cotyledon pavement cells of the examined growth phase. This also indicates that the mechanical homogeneity of the mutant cell wall is not significantly different from that of the wild-type wall to a level sufficient to influence the simulation results.

While other possible advantages for plant pavement cells to adopt the jigsaw-puzzle shapes pertain to multicellular processes (see the introduction of this study), the mechanical stress hypothesis operates on a single cell level. Simulation models suggest that complex cell geometry with frequent lobes effectively reduces the maximal wall stress in the cell center by dispersing the stress to the indented region between lobes (Sampathkumar et al., 2014a; Sapala et al., 2018). Shallow lobed cells would experience high wall stress at the cell center as the cell area increases and would bulge outward, which is the exact phenotype seen in the *bpp* pavement cells. The outer periclinal wall with high mechanical stress may be vulnerable to biotic and abiotic stresses that damage cell wall integrity (Engelsdorf et al., 2018). The *bpp* cells will provide useful plant materials with which to explore the biological meanings of lobe development.

MATERIALS AND METHODS

Plant Materials and Growth Conditions

Arabidopsis (*Arabidopsis thaliana*) ecotype Columbia (Col) was used in all experiments. Sterilized seeds were sown on Arabidopsis agar medium (Nakamura et al., 2004), and stratified at 4°C in the dark for 4 d. After stratification, the seeds were germinated and grown in vertical orientation at 23°C with a long photoperiod (16-h light period, 8-h dark period). The GFP-TUB6 microtubule marker line (Nakamura et al., 2004) was crossed to *bpp* mutants, and transgenic Arabidopsis plants expressing a GFP-tagged BPP protein were crossed to the mCherry-TUB6 line (Fujita et al., 2013). The floral dip method (Clough and Bent, 1998) with *Agrobacterium tumefaciens* GV3101 (pMP90) strains was used to generate transgenic Arabidopsis lines. For complementation assays, *gGFP-BPP1* and *gGFP-BPP5* constructs were transformed into *bpp15* and *bpp125* mutants.

Vector Construction

Full-length complementary DNAs of *BPP1*, *BPP2*, *BPP3*, and *BPP4* were placed under the control of the *UBIQUITIN 10* promoter, and cloned into the pBIN40 vector. Genomic fragments containing *BPP1* and *BPP5*, along with 2,550-bp and 2,2562-bp 5′-fragments, respectively, upstream from their translation start *ATG*s, and 969-bp and 874-bp 3′-fragments, respectively, downstream from the translation terminating stop codons, were cloned into pBIN40, and *GFP* was inserted before the translation initiation *ATG* codons to generate *gGFP-BPP1* (7,063 bp) and *gGFP-BPP5* (8,635 bp). For the promoter-GUS analysis, 2.6 kb 5′-regions upstream of seven *BPP* genes were cloned into pGWB3 (Nakagawa et al., 2007). See Supplemental Table S2 for PCR primer sequences.

Phylogenetic Analysis

Multiple alignment was performed using a Multiple Alignment tool from the program Fast Fourier Transform (Katoh et al., 2017), and the evolutionary history was inferred using the Neighbor-Joining method (Saitou and Nei, 1987). The percentage of replicate trees, in which the associated taxa clustered together in the bootstrap test (1,000 replicates), are shown next to the branches (Felsenstein, 1985). The evolutionary distances were computed using the Poisson correction method (Zuckerkandl and Pauling, 1965) and are in the units of the number of amino acid substitutions per site. Evolutionary analyses were conducted in the program MEGA7 (Kumar et al., 2016).

Reverse Transcription-PCR

Total RNA from different plant tissues were extracted using RNAeasy Plant Mini kit (Qiagen). First-strand complementary DNA was synthesized from 1 μg of total RNA by using SuperScript II reverse transcriptase (Life Technologies). *ACT8* gene expression was used as control. Primer sequences are provided in Supplemental Table S2. PCR was done under standard conditions of 28 cycles and PCR products were analyzed by using agarose gel electrophoresis and staining with ethidium bromide. See Supplemental Table S2 for PCR primer sequences.

Genomic PCR

Gene-specific primers were designed on the *BPP* genes flanking the expected T-DNA insertion sites. Combination of a pair of gene-specific primers (LP and RP) and the T-DNA border-site primer were used to amplify the target *BPP* genes. See Supplemental Table S2 for PCR primer sequences.

GUS Staining

GUS staining was done according to Jefferson et al. (1987). More than three independent transgenic lines were analyzed for each *BPP* promoter, and gave similar staining patterns. A MVX10 Stereo Microscope (Olympus) was used to acquire the GUS-stained images.

Analysis of Cell Shapes

Excised cotyledons were submerged in a propidium iodide solution (1 mg mL^{-1}; Sigma-Aldrich) for 1 min, rinsed with distilled water, and analyzed using an inverted microscope (ECLIPSE Ti; Nikon) with a spinning-disk confocal unit (CSU-XI; Yokogawa) connected to an EM-CCD camera (iXon3 DU897; Andor). Images were acquired using CFI S Plan Fluor objective lenses (Nikon; 40× for 1 and 2 DAG, 20× for 3 and 5 DAG, and 10× for 8 DAG). Excitation energy was supplied by lasers (Andor) at 561 nm with a 617/73 filter. PaCeQuant (Möller et al., 2017) was used to segment cell shapes from the images and obtain cell shape parameters. Lobe numbers were also estimated by using LobeFinder (Wu et al., 2016) after applying Bezier spline to the cell edges to smooth the pixel-wise roughness at the edges. Statistical significance was determined using a paired two-sample Student's *t-test* using the software Microsoft Excel.

To measure LEC and the cell height, cotyledons stained with propidium iodide were mounted within a chamber made by stacking several sheets of iSpacer (SunJin Lab) in water. Stack images of 1,024/1,024 pixels (0.621 μm/pixel) were obtained using an inverted microscope (FLUOVIEW FV1000; Olympus) and a UPLSAPO 20×/0.75 objective lens (Olympus), with excitation at 561 nm using a 617/73 filter. Projection images of pavement cells were generated by the *z*-projection program of ImageJ/Fiji (https://fiji.sc/), with a projection-type parameter of maximum intensity or sum slices. The PaCeQuant plugin (Möller et al., 2017) was then used to generate cell segmentation images, with a cell-size parameter of 1,000–100,000 pixel units. The largest 30 cells from each cotyledon were used for the analysis to exclude stomata and those in the stomatal lineage, and three cotyledons (a total of 90 cells) were analyzed for each genotype at each time point. Because PaCeQuant frequently failed to correctly define the cell contour for wild-type pavement cells at 8 DAG, only 30 cells were analyzed from three wild-type cotyledons at 8 DAG after assuring the correct cell segmentation. LEC was calculated by the Max Inscribed Circle program in the MorphoLibJ plugin (Legland et al., 2016). The maximum height of pavement cells was measured by generating a resliced image of the x,z plane that intersects the center coordinate of the LEC.

Imaging of Fluorescent Proteins

Fluorescence images were captured using a spinning disk confocal head (CSU-XI; Yokogawa Electric) mounted on an inverted microscope (ECLIPSE Ti; Nikon) with a numerical aperture oil-immersion objective (Apo TIRF 60X/1.49; Nikon). Excitation energy was supplied by lasers (Andor) at 488 nm with a 520/35 filter for GFP, and at 561 nm with a 617/73 filter for mCherry. All images were taken by sequential acquisition of single channels. For dual-color visualization, mCherry was first excited and its emission signals collected with an exposure time of 0.2 s, after which GFP was excited and its emission signals taken with an exposure time of 0.5 s. The *z*-stack images of cells were acquired by superimposing image slices with an interval of 0.2 μm. Time-lapse imaging of anticlinal microtubules was done in 2-DAG whole seedlings as described in Belteton et al. (2018). The cortical density of periclinal microtubules was analyzed as reported in Belteton et al. (2018). The *z*-stack projections of cortical microtubules in Figure 8 and Supplemental Figure S16 were generated by stacking 31 slices (wild type) and 70 slices (*bpp125*) with Stack Focuser (kernel 9) in the software ImageJ (https://imagej.nih.gov/ij/plugins/stack-focuser.html).

Quantification of Periclinal Splayed Microtubules with Respect to Wall Curvature Using MtCurv

Outline

Using confocal images of microtubules at the midplane of a cell, a closed curve of the cell contour was manually drawn (Fig. 6A, i) and the contour was shrunk by a width of 5 pixels (1.09 μm; Fig. 6A, ii). The shrunk contour (defined here as the LOI) was used for the following analysis. The curvature along the LOI was calculated at 1-pixel (0.218 μm) steps as a reciprocal of the radius of a curvature circle, which is a circle passing through the three adjacent vertices (P_{i-1}, P_i, and P_{i+1}) on the LOI (Fig. 6A, iii and iv). Simultaneously, *XY* coordinates of the center of a curvature circle were measured to score the sides of the anticlinal cell wall as concave or convex. If the circle center is located inside the LOI, the region is concave, and vice versa. Thus, we quantitatively evaluated the curvature of the cell contour based on a list of assigned curvature values along the pixels comprising the LOI.

Intensity, coherency, and orientation of microtubules were measured along the LOI at locations that were 1 pixel (0.218 μm) apart, using a maximum intensity projection image obtained from serial optical sections and the ImageJ plugin OrientationJ (http://bigwww.epfl.ch/demo/orientation/; Gaussian window σ = 3 [pix], Cubic Spline Gradient; Rezakhaniha et al., 2012). The maximum signal intensity in each cell was set to 1.0, and all the intensities were shown in relative values. All measurements of the signed curvature and the three microtubule metrics were performed by the software ImageJ. The relationship among the values at the corresponding pixel locations was investigated using the software package R (https://rstudio.com/).

Judgement of the concave and convex sides

The LOI was traced either clockwise or counterclockwise. When the LOI was traced counterclockwise, the left-side location of the curvature circle indicated that the vertex P_i is located on the convex side, whereas its right-side location indicated that it was on the concave side (Supplemental Fig. S18A). Clockwise tracing gave the opposite results. The direction of tracing was determined based on the sign obtained when calculating the area A as the sum of triangles surrounded by the coordinate origin $O(0,0)$ and each side $\overline{P_iP_{i+1}}$ of the polygon LOI. A is given by the following equation:

$$A=\sum_{i=0}^{n}\frac{\overrightarrow{OP_i}\times\overrightarrow{OP_{i+1}}}{2}=\frac{1}{2}\sum_{i=0}^{n}\left(x_iy_{i+1}-y_ix_{i+1}\right)$$

$$\overrightarrow{OP_i}=\left(x_i,\ y_i\right)$$

$$\overrightarrow{OP_{n+1}}=\overrightarrow{OP_0}=(x_0,y_0)$$

where n = the number of vertices on LOI.

If the result of the above equation is positive, the direction of tracing the vertex is clockwise (Supplemental Fig. S18B). If it is negative, it is counterclockwise. Note that the coordinate system of ImageJ displays a downward *y*-axis.

The below vector product is calculated to determine whether the center $C_i(X_i,Y_i)$ of the curvature circle is located on the left $(\theta_i>0)$ or right $(\theta_i<0)$ side relative to the direction of $\overrightarrow{P_iP_{i-1}}$ on LOI,

$$|\overrightarrow{P_{i-1}C_i}\times\overrightarrow{P_{i-1}P_i}|=|\overrightarrow{P_{i-1}C_i}||\overrightarrow{P_{i-1}P_i}|\sin\theta_i,\quad -\frac{\pi}{2}<\theta_i<\frac{\pi}{2}$$

$$\sin\theta_i=\frac{(X_i-x_{i-1})(y_i-y_{i-1})-(Y_i-y_{i-1})(x_i-x_{i-1})}{|\overrightarrow{P_{i-1}C_i}||\overrightarrow{P_{i-1}P_i}|}$$

where if $(X_i-x_{i-1})(y_i-y_{i-1})-(Y_i-y_{i-1})(x_i-x_{i-1})>0$, then $\sin\theta_i>0$, that is $0<\theta_i<\frac{\pi}{2}$. By contrast, if $(X_i-x_{i-1})(y_i-y_{i-1})-(Y_i-y_{i-1})(x_i-x_{i-1})<0$, then $\sin\theta_i<0$, that is $-\frac{\pi}{2}<\theta_i<0$.

The following equation using the Math.signum function in JAVA (https://docs.oracle.com/javase/8/docs/api/java/lang/Math.html) is used to determine the sign of the curvature:

$$\text{Math.signum(x)} = \begin{cases} -1 & if\ x<0 \\ 0 & if\ x=0 \\ 1 & if\ x>0 \end{cases}$$

A signed radius $signed\_R_i$ of the curvature circle at the P_i vertex is therefore defined by the following equation:

$$signed\_R_i = \text{signum}(A) * \text{signum}\big((X_i - x_{i-1})(y_i - y_{i-1}) - (Y_i - y_{i-1})(x_i - x_{i-1})\big) * R_i$$

Conversion of the orientation value

"Orientation" output by OrientationJ is a directional value, and is defined by the inclination to the horizontal direction (*x*-axis direction) of an image (Supplemental Fig. S18C). This value depends on the coordinate system. Because the *y*-axis was directed downward in the pixel coordinate system and because our analysis focused on the orientation of microtubules with respect to the cell contour, the orientation value was adjusted based on the normal direction to the cell contour at each vertex, as shown below. To treat the *xy* coordinate as the right-hand system, the sign of a *y* coordinate is inverted. The angle $\boldsymbol{\varphi}_i$ that the normal vector $\overrightarrow{P_iC_i}$ $[(X_i - x_i, (-Y_i) - (-y_i)) = (X_i - x_i, y_i - Y_i)]$ makes with the *x*-axis is calculated using the *atan2*(*x*, *y*) function:

$$\varphi_i = atan2\big(X_i - x_i,\ y_i - Y_i\big)$$
$$-\pi < \varphi_i \le \pi$$

Subsequently, the inclination φ_{ori_i} of the normal line at the P_i vertex is calculated according to the following equation. The range of φ_{ori_i} is defined with the same range as Orientation α_i processed by OrientationJ:

$$\varphi_{ori\_i} = \varphi_i + \Big(-\pi < \varphi_i \le -\frac{\pi}{2}\Big) * \pi - \Big(\frac{\pi}{2} < \varphi_i \le \pi\Big) * \pi$$
$$-\frac{\pi}{2} < \varphi_{ori\_i} \le \frac{\pi}{2}$$

Next, α_i is converted to the angle α_{dif_i} with respect to the normal line at the P_i vertex using the following equation:

$$\alpha_{dif\_i} = \alpha_i - \varphi_{ori\_i} + \Big(-\pi < \alpha_i - \varphi_{ori\_i} \le -\frac{\pi}{2}\Big) * \pi - \Big(\frac{\pi}{2} < \alpha_i - \varphi_{ori\_i} \le \pi\Big) * \pi$$
$$= \alpha_i - \varphi_i + k\pi \quad (k = -2, -1, 0, 1, 2)$$
$$-\frac{\pi}{2} < \alpha_{dif\_i} \le \frac{\pi}{2}$$

Normalization of orientation and intensity values

The following conversion equation is used to normalize α_{dif_i} so that the normalized value for orientation is the highest (i.e. 1) at $\alpha_i = 0$ and the lowest (i.e. 0) at $\alpha_i = \pm\frac{\pi}{2}$. Normalization was performed on each cell individually:

$$Ori_{norm\_i} = \frac{1}{2}\big(\cos 2\alpha_{dif\_i} + 1\big)$$
$$= \frac{1}{2}\big(\cos 2(\alpha_i - \varphi_i + k\pi) + 1\big)$$
$$= \frac{1}{2}\big(\cos 2(\alpha_i - \varphi_i) + 1\big)$$
$$0 \le Ori_{norm\_i} \le 1$$

The intensity value Int_i at the P_i vertex was normalized to the relative value Int_{rel_i} after dividing by the maximum value Int_{max} as follows:

$$Int_{rel\_i} = Int_i / Int_{max}$$
$$0 \le Int_{rel\_i} \le 1$$

Quantification of Anticlinal Microtubule Bundles using BQuant

The fluorescence intensity of microtubule bundle was quantified as a one-dimensional sequence $I(x)$ by line-scanning the image (line width = 5 pixels) and eliminating background trend noise in the sequence using the rolling-ball algorithm (2-pixel radius with sliding paraboloid approximation). These image preprocessing steps were performed using ImageJ (Fig. 7, B–D). We developed the mathematical model of the sequence as the superimposition of the Gaussian-like fluorescence intensity of a single microtubule bundle and estimated the model parameters by Bayesian framework. Letting m_i, s_i, and h_i be the parameters of center coordinate, width, and height of the *i*th Gaussian, respectively, the fluorescence intensity at the coordinate X was modeled as $f(x|m_i, s_i, h_i) = h_i \exp\{-(x - m_i)^2 / 2s_i^2\}$. Consequently, the superimposition of the functions becomes $\sum_i f(x|m_i, s_i, h_i)$. Supposing Gaussian observation noise between the quantified data and the mathematical model, the likelihood function for the quantified sequence $I(x)$ can be written as the product of the Gaussian distributions over all observation coordinates $\{x_j\}$, $\prod_j N(I(x=x_j)|\sum_i f(x_j|m_i, s_i, h_i), \sigma^2)$, where σ represents the size of observation noise. To strictly evaluate the likelihood, we set $\sigma = 10$, which is much smaller than the scale of the quantified values (up to several thousand). We introduced the Gaussian priors on the model parameters, $N(m_i|\mu_i, 0.01^2)$, $N(s_i|2, 2^2)$, and $N(h_i|I(x=\mu_i), 500^2)$, which means that the microtubule bundle center (m_i), width (s_i), and height (h_i) are constrained so as to take the values around the values given in advance, μ_i, 2, and $I(x=\mu_i)$, respectively. We strongly constrained the center (SD = 0.01 (pixel)), but weakly constrained width (SD = 2 [pixel]) and height (SD = 500 [a.u.]). The parameter of the center (μ_i) was decided as the place where a microtubule is considered to be present: namely, the point with the positive peak of the sequence, the point with the smallest slope in the monotonous and stepwise increasing sequence, or the point with the largest slope in the monotonous and stepwise decreasing sequence. Then we computed the model parameters to maximize the mode of the posterior, $P(m_i, s_i, h_i|I)$, which is proportional to the product of the likelihood and the priors. Computations were performed with the software MATLAB (The MathWorks).

Statistical Analyses

Statistical analyses were performed using Microsoft Excel and "R" software. The data are presented as mean ± SD, and *n* values are shown in the figure legends. For boxplots, the bottom and top of each box represent the first and third quartiles of the distribution of the Kendall correlation coefficient, respectively. The horizontal line inside each box is the median (second quartile), and the diamond represents the average. The whiskers range between $\pm 1.58\ IQR\ n^{-1/2}$, where *IQR* is the interquartile range and n = number of points in the distributions. Data points outside this range are considered as outliers and are indicated as dots. *ns* indicates not significant, $^{*}P \le 0.05$, $^{**}P \le 0.01$, $^{***}P \le 0.001$. Student's *t*-test (two-tailed) was used to compare means for two groups, whereas one-way ANOVA with Dunnett's multiple-comparison test was performed to compare means from several groups against a control group mean. Welch's two sample *t*-test was used to compare microtubule metrics between wild-type and the mutant cells.

Accession Numbers

Sequence data from this article can be found in the GenBank/European Molecular Biology Laboratory data libraries under the following accession numbers: At2g40070 (*BPP1*), At3g09000 (*BPP2*), At5g01280 (*BPP3*), At2g38160 (*BPP4*), At1g27850 (*BPP5*), At3g08670 (*BPP6*), and At3g51540 (*BPP7*). The reference numbers of the T-DNA insertion alleles are as follows: SALK_011272 (*bpp1-1*), SALK_114501 (*bpp1-3*), SALK_028501 (*bpp1-4*), SALK_117868 (*bpp2-5*), SALK_205505 (*bpp5-1*), and SALK_098323 (*bpp5-2*).

Supplemental Data

The following supplemental materials are available.

Supplemental Figure S1. Phylogenetic tree of BPP family proteins based on their full-length sequences.

Supplemental Figure S2. Subcellular localization of GFP-BPPs.

Supplemental Figure S3. Expression patterns of *BPP* promoters.

Supplemental Figure S4. Expression patterns of *BPP* genes analyzed by reverse transcription-PCR.

Supplemental Figure S5. Expression patterns of *BPP* genes in Genevestigator.

Supplemental Figure S6. *BPP* knockout mutants.

Supplemental Figure S7. BPP expression in knock-out mutants.

Supplemental Figure S8. Phenotypes of *bpp* mutants.

Supplemental Figure S9. Complementation analyses.

Supplemental Figure S10. Lobe types in pavement cells at 5 DAG.

Supplemental Figure S11. Ratio of lobe length to lobe width.

Supplemental Figure S12. Analysis of cell curvature and microtubule parameters (intensity, coherency, and orientation) on the LOI.

Supplemental Figure S13. Distributions of microtubule signal intensities over the cell curvature.

Supplemental Figure S14. Spatial abundance of periclinal microtubules based on splayed microtubule index.

Supplemental Figure S15. Persistence plots of microtubule signals beneath anticlinal wall segments.

Supplemental Figure S16. Distribution of individual modeled peak widths.

Supplemental Figure S17. Microtubule patterns in 5-DAG *bpp125* cells.

Supplemental Figure S18. Illustration related to the formula used for MtCurv.

Supplemental Table S1. BPP-family protein in plants.

Supplemental Table S2. DNA primer sequences.

ACKNOWLEDGMENTS

We thank the Salk Institute for providing the T-DNA insertional alleles.

Received July 10, 2019; accepted September 30, 2019; published October 10, 2019.

LITERATURE CITED

Akita K, Higaki T, Kutsuna N, Hasezawa S (2015) Quantitative analysis of microtubule orientation in interdigitated leaf pavement cells. Plant Signal Behav **10:** e1024396

Altartouri B, Bidhendi AJ, Tani T, Suzuki J, Conrad C, Chebli Y, Liu N, Karunakaran C, Scarcelli G, Geitmann A (2019) Pectin chemistry and cellulose crystallinity govern pavement cell morphogenesis in a multi-step mechanism. Plant Physiol **181:** 127–141

Ambrose JC, Shoji T, Kotzer AM, Pighin JA, Wasteneys GO (2007) The Arabidopsis CLASP gene encodes a microtubule-associated protein involved in cell expansion and division. Plant Cell **19:** 2763–2775

Armour WJ, Barton DA, Law AM, Overall RL (2015) Differential growth in periclinal and anticlinal walls during lobe formation in Arabidopsis cotyledon pavement cells. Plant Cell **27:** 2484–2500

Baskin TI (2005) Anisotropic expansion of the plant cell wall. Annu Rev Cell Dev Biol **21:** 203–222

Belteton SA, Sawchuk MG, Donohoe BS, Scarpella E, Szymanski DB (2018) Reassessing the roles of PIN proteins and anticlinal microtubules during pavement cell morphogenesis. Plant Physiol **176:** 432–449

Bidhendi AJ, Altartouri B, Gosselin FP, Geitmann A (2019) Mechanical stress initiates and sustains the morphogenesis of wavy leaf epidermal cells. Cell Reports **28:** 1237–1250.e6

Clough SJ, Bent AF (1998) Floral dip: A simplified method for Agrobacterium-mediated transformation of *Arabidopsis thaliana*. Plant J **16:** 735–743

Cosgrove DJ (2014) Re-constructing our models of cellulose and primary cell wall assembly. Curr Opin Plant Biol **22:** 122–131

Elsner J, Lipowczan M, Kwiatkowska D (2018) Differential growth of pavement cells of *Arabidopsis thaliana* leaf epidermis as revealed by microbead labeling. Am J Bot **105:** 257–265

Elsner J, Michalski M, Kwiatkowska D (2012) Spatiotemporal variation of leaf epidermal cell growth: A quantitative analysis of *Arabidopsis thaliana* wild-type and triple cyclinD3 mutant plants. Ann Bot **109:** 897–910

Eng RC, Sampathkumar A (2018) Getting into shape: The mechanics behind plant morphogenesis. Curr Opin Plant Biol **46:** 25–31

Engelsdorf T, Gigli-Bisceglia N, Veerabagu M, McKenna JF, Vaahtera L, Augstein F, Van der Does D, Zipfel C, Hamann T (2018) The plant cell wall integrity maintenance and immune signaling systems cooperate to control stress responses in *Arabidopsis thaliana*. Sci Signal **11:** eaao3070

Felsenstein J (1985) Confidence limits on phylogenies: An approach using the bootstrap. Evolution **39:** 783–791

Forouzesh E, Goel A, Mackenzie SA, Turner JA (2013) In vivo extraction of Arabidopsis cell turgor pressure using nanoindentation in conjunction with finite element modeling. Plant J **73:** 509–520

Fu Y, Gu Y, Zheng Z, Wasteneys G, Yang Z (2005) Arabidopsis interdigitating cell growth requires two antagonistic pathways with opposing action on cell morphogenesis. Cell **120:** 687–700

Fujita S, Pytela J, Hotta T, Kato T, Hamada T, Akamatsu R, Ishida Y, Kutsuna N, Hasezawa S, Nomura Y, et al (2013) An atypical tubulin kinase mediates stress-induced microtubule depolymerization in Arabidopsis. Curr Biol **23:** 1969–1978

Glover BJ (2000) Differentiation in plant epidermal cells. J Exp Bot **51:** 497–505

Hamada T, Nagasaki-Takeuchi N, Kato T, Fujiwara M, Sonobe S, Fukao Y, Hashimoto T (2013) Purification and characterization of novel microtubule-associated proteins from Arabidopsis cell suspension cultures. Plant Physiol **163:** 1804–1816

Higaki T, Kutsuna N, Sano T, Kondo N, Hasezawa S (2010) Quantification and cluster analysis of actin cytoskeletal structures in plant cells: Role of actin bundling in stomatal movement during diurnal cycles in Arabidopsis guard cells. Plant J **61:** 156–165

Jacques E, Verbelen JP, Vissenberg K (2014) Review on shape formation in epidermal pavement cells of the Arabidopsis leaf. Funct Plant Biol **41:** 914–921

Jefferson RA, Kavanagh TA, Bevan MW (1987) GUS fusions: Beta-glucuronidase as a sensitive and versatile gene fusion marker in higher plants. EMBO J **6:** 3901–3907

Jordan BM, Dumais J (2010) Biomechanics of plant cell growth. In Encyclopedia of Life Sciences (*eLS*). John Wiley & Sons, Ltd, Chichester

Katoh K, Rozewicki J, Yamada KD (2017) MAFFT online service: Multiple sequence alignment, interactive sequence choice and visualization. Brief Bioinform **20:** 1160–1166

Kierzkowski D, Routier-Kierzkowska AL (2019) Cellular basis of growth in plants: Geometry matters. Curr Opin Plant Biol **47:** 56–63

Kirik V, Herrmann U, Parupalli C, Sedbrook JC, Ehrhardt DW, Hülskamp M (2007) CLASP localizes in two discrete patterns on cortical microtubules and is required for cell morphogenesis and cell division in Arabidopsis. J Cell Sci **120:** 4416–4425

Kotzer AM, Wasteneys GO (2006) Mechanisms behind the puzzle: microtubule-microfilament cross-talk in pavement cell formation. Can J Bot **84:** 594–603

Kumar S, Stecher G, Tamura K (2016) MEGA7: Molecular Evolutionary Genetics Analysis version 7.0 for bigger datasets. Mol Biol Evol **33:** 1870–1874

Kutschera U (2008) The growing outer epidermal wall: Design and physiological role of a composite structure. Ann Bot **101:** 615–621

Lee YK, Kim GT, Kim IJ, Park J, Kwak SS, Choi G, Chung WI (2006) LONGIFOLIA1 and LONGIFOLIA2, two homologous genes, regulate longitudinal cell elongation in Arabidopsis. Development **133:** 4305–4314

Legland D, Arganda-Carreras I, Andrey P (2016) MorphoLibJ: Integrated library and plugins for mathematical morphology with ImageJ. Bioinformatics **32:** 3532–3534

Liang H, Zhang Y, Martinez P, Rasmussen CG, Xu T, Yang Z (2018) The microtubule-associated protein IQ67 DOMAIN5 modulates microtubule dynamics and pavement cell shape. Plant Physiol **177:** 1555–1568

Lin D, Cao L, Zhou Z, Zhu L, Ehrhardt D, Yang Z, Fu Y (2013) Rho GTPase signaling activates microtubule severing to promote microtubule ordering in Arabidopsis. Curr Biol **23:** 290–297

Majda M, Grones P, Sintorn IM, Vain T, Milani P, Krupinski P, Zagórska-Marek B, Viotti C, Jönsson H, Mellerowicz EJ, et al (2017) Mechanochemical polarization of contiguous cell walls shapes plant pavement cells. Dev Cell **43:** 290–304.e4

Mitra D, Klemm S, Kumari P, Quegwer J, Möller B, Poeschl Y, Pflug P, Stamm G, Abel S, Bürstenbinder K (2019) Microtubule-associated

protein IQ67 DOMAIN5 regulates morphogenesis of leaf pavement cells in *Arabidopsis thaliana*. J Exp Bot **70:** 529–543

Möller B, Poeschl Y, Plötner R, Bürstenbinder K (2017) PaCeQuant: A tool for high-throughput quantification of pavement cell shape characteristics. Plant Physiol **175:** 998–1017

Nakagawa T, Kurose T, Hino T, Tanaka K, Kawamukai M, Niwa Y, Toyooka K, Matsuoka K, Jinbo T, Kimura T (2007) Development of series of gateway binary vectors, pGWBs, for realizing efficient construction of fusion genes for plant transformation. J Biosci Bioeng **104:** 34–41

Nakamura M, Naoi K, Shoji T, Hashimoto T (2004) Low concentrations of propyzamide and oryzalin alter microtubule dynamics in Arabidopsis epidermal cells. Plant Cell Physiol **45:** 1330–1334

Panteris E, Apostolakos P, Galatis B (1994) Sinuous ordinary epidermal cells: Behind several patterns of waviness, a common morphogenetic mechanism. New Phytol **127:** 771–780

Panteris E, Galatis B (2005) The morphogenesis of lobed plant cells in the mesophyll and epidermis: organization and distinct roles of cortical microtubules and actin filaments. New Phytol **167:** 721–732

Qiu JL, Jilk R, Marks MD, Szymanski DB (2002) The Arabidopsis SPIKE1 gene is required for normal cell shape control and tissue development. Plant Cell **14:** 101–118

Rezakhaniha R, Agianniotis A, Schrauwen JTC, Griffa A, Sage D, Bouten CVC, van de Vosse FN, Unser M, Stergiopulos N (2012) Experimental investigation of collagen waviness and orientation in the arterial adventitia using confocal laser scanning microscopy. Biomech Model Mechanobiol **11:** 461–473

Robinson S, Kuhlemeier C (2018) Global compression reorients cortical microtubules in Arabidopsis hypocotyl epidermis and promotes growth. Curr Biol **28:** 1794–1802.e2

Saitou N, Nei M (1987) The neighbor-joining method: A new method for reconstructing phylogenetic trees. Mol Biol Evol **4:** 406–425

Sampathkumar A, Krupinski P, Wightman R, Milani P, Berquand A, Boudaoud A, Hamant O, Jönsson H, Meyerowitz EM (2014a) Subcellular and supracellular mechanical stress prescribes cytoskeleton behavior in Arabidopsis cotyledon pavement cells. eLife **3:** e01967

Sampathkumar A, Yan A, Krupinski P, Meyerowitz EM (2014b) Physical forces regulate plant development and morphogenesis. Curr Biol **24:** R475–R483

Sapala A, Runions A, Routier-Kierzkowska AL, Das Gupta M, Hong L, Hofhuis H, Verger S, Mosca G, Li CB, Hay A, et al (2018) Why plants make puzzle cells, and how their shape emerges. eLife **7:** e32794

Sapala A, Runions A, Smith RS (2019) Mechanics, geometry and genetics of epidermal cell shape regulation: Different pieces of the same puzzle. Curr Opin Plant Biol **47:** 1–8

Szymanski DB (2014) The kinematics and mechanics of leaf expansion: New pieces to the Arabidopsis puzzle. Curr Opin Plant Biol **22:** 141–148

Verger S, Long Y, Boudaoud A, Hamant O (2018) A tension-adhesion feedback loop in plant epidermis. eLife **7:** e34460

Vőfély RV, Gallagher J, Pisano GD, Bartlett M, Braybrook SA (2019) Of puzzles and pavements: A quantitative exploration of leaf epidermal cell shape. New Phytol **221:** 540–552

Wu TC, Belteton SA, Pack J, Szymanski DB, Umulis DM (2016) LobeFinder: A convex hull-based method for quantitative boundary analyses of lobed plant cells. Plant Physiol **171:** 2331–2342

Yanagisawa M, Desyatova AS, Belteton SA, Mallery EL, Turner JA, Szymanski DB (2015) Patterning mechanisms of cytoskeletal and cell wall systems during leaf trichome morphogenesis. Nat Plants **1:** 15014

Zhang C, Halsey LE, Szymanski DB (2011) The development and geometry of shape change in *Arabidopsis thaliana* cotyledon pavement cells. BMC Plant Biol **11:** 27

Zuckerkandl E, Pauling L (1965) Evolutionary divergence and convergence in proteins. In V Bryson, and HJ Vogel, eds, Evolving Genes and Proteins. Academic Press, New York, pp 97–166